

Supplementary Materials for **Beyond triplet: Unconventional superconductivity in a spin-3/2 topological semimetal**

Hyunsoo Kim, Kefeng Wang, Yasuyuki Nakajima, Rongwei Hu, Steven Ziemak, Paul Syers, Limin Wang, Halyna Hodovanets, Jonathan D. Denlinger, Philip M. R. Brydon, Daniel F. Agterberg, Makariy A. Tanatar, Ruslan Prozorov, Johnpierre Paglione

Published 6 April 2018, *Sci. Adv.* **4**, eaao4513 (2018)

DOI: 10.1126/sciadv.aao4513

This PDF file includes:

- fig. S1. Band structure of YPtBi.
- fig. S2. Photon-dependent ARPES of Bi-terminated YPtBi(111).
- fig. S3. Normalized magnitude of each gap along high symmetry points.
- fig. S4. Superfluid density in YPtBi and other well-known superconductors.
- fig. S5. Angle-dependent magnetoresistance in YPtBi.
- fig. S6. Angle-dependent frequency of Shubnikov–de Haas quantum oscillation in YPtBi.
- fig. S7. Temperature-dependent quantum oscillations with $\theta = 90^\circ$ and $\phi = 0^\circ$.

SPIN-3/2 PAIRING

In YPtBi, the electronic Γ_8 representation responsible for the states near the chemical potential can be described by a $j = 3/2$ basis with four basis elements: $\{|\frac{3}{2}\rangle, |\frac{1}{2}\rangle, |-\frac{1}{2}\rangle, |-\frac{3}{2}\rangle\}$. Physically this basis stems from $l = 1$ p -states coupled to $s = 1/2$ spin. In this direct product space, the basis elements can be expressed as

$$|\frac{3}{2}\rangle = \frac{1}{\sqrt{2}}[-|p_x, \frac{1}{2}\rangle - i|p_y, \frac{1}{2}\rangle] \quad (\text{S1})$$

$$|\frac{1}{2}\rangle = \frac{1}{\sqrt{6}}[2|p_z, \frac{1}{2}\rangle - |p_x, -\frac{1}{2}\rangle - i|p_y, -\frac{1}{2}\rangle] \quad (\text{S2})$$

$$|-\frac{1}{2}\rangle = \frac{1}{\sqrt{6}}[2|p_z, -\frac{1}{2}\rangle + |p_x, \frac{1}{2}\rangle - i|p_y, \frac{1}{2}\rangle] \quad (\text{S3})$$

$$|-\frac{3}{2}\rangle = \frac{1}{\sqrt{2}}[|p_x, -\frac{1}{2}\rangle - i|p_y, -\frac{1}{2}\rangle] \quad (\text{S4})$$

Cooper pairs can be constructed from these Γ_8 states. In particular using the angular momentum addition rule: $\frac{3}{2} \otimes \frac{3}{2} = 3 \oplus 2 \oplus 1 \oplus 0$, we can classify the sixteen possible Cooper pairs as follows

$J = 0$ singlet state

$$|J = 0, m_J = 0\rangle = \frac{1}{2}\left(|\frac{3}{2}, -\frac{3}{2}\rangle - |-\frac{3}{2}, \frac{3}{2}\rangle - |\frac{1}{2}, -\frac{1}{2}\rangle + |-\frac{1}{2}, \frac{1}{2}\rangle\right) \quad (\text{S5})$$

$J = 1$ triplet states

$$\begin{aligned} |J = 1, m_J = 1\rangle &= \frac{1}{\sqrt{10}}\left(\sqrt{3}|\frac{3}{2}, -\frac{1}{2}\rangle - 2|\frac{1}{2}, \frac{1}{2}\rangle + \sqrt{3}|-\frac{1}{2}, \frac{3}{2}\rangle\right) \\ |J = 1, m_J = 0\rangle &= \frac{1}{\sqrt{20}}\left(3|\frac{3}{2}, -\frac{3}{2}\rangle - |\frac{1}{2}, -\frac{1}{2}\rangle - |-\frac{1}{2}, \frac{1}{2}\rangle + 3|-\frac{3}{2}, \frac{3}{2}\rangle\right) \\ |J = 1, m_J = -1\rangle &= \frac{1}{\sqrt{10}}\left(\sqrt{3}|-\frac{3}{2}, \frac{1}{2}\rangle - 2|-\frac{1}{2}, -\frac{1}{2}\rangle + \sqrt{3}|\frac{1}{2}, -\frac{3}{2}\rangle\right) \end{aligned} \quad (\text{S6})$$

$J = 2$ quintet states

$$\begin{aligned} |J = 2, m_J = 2\rangle &= \frac{1}{\sqrt{2}}\left(|\frac{3}{2}, \frac{1}{2}\rangle - |-\frac{1}{2}, \frac{3}{2}\rangle\right) \\ |J = 2, m_J = 1\rangle &= \frac{1}{\sqrt{2}}\left(|\frac{3}{2}, -\frac{1}{2}\rangle - |-\frac{1}{2}, \frac{3}{2}\rangle\right) \\ |J = 2, m_J = 0\rangle &= \frac{1}{2}\left(|\frac{3}{2}, -\frac{3}{2}\rangle + |\frac{1}{2}, -\frac{1}{2}\rangle - |\frac{1}{2}, -\frac{1}{2}\rangle - |-\frac{3}{2}, \frac{3}{2}\rangle\right) \\ |J = 2, m_J = -1\rangle &= \frac{1}{\sqrt{2}}\left(|-\frac{3}{2}, \frac{1}{2}\rangle - |-\frac{1}{2}, -\frac{3}{2}\rangle\right) \\ |J = 2, m_J = -2\rangle &= \frac{1}{\sqrt{2}}\left(|-\frac{3}{2}, -\frac{1}{2}\rangle - |-\frac{1}{2}, -\frac{3}{2}\rangle\right) \end{aligned} \quad (\text{S7})$$

and $J = 3$ septet states

$$\begin{aligned}
|J = 3, m_J = 3\rangle &= |\frac{3}{2}, \frac{3}{2}\rangle \\
|J = 3, m_J = 2\rangle &= \frac{1}{\sqrt{2}}\left(|\frac{3}{2}, \frac{1}{2}\rangle + |\frac{1}{2}, \frac{3}{2}\rangle\right) \\
|J = 3, m_J = 1\rangle &= \frac{1}{\sqrt{5}}\left(|\frac{3}{2}, -\frac{1}{2}\rangle + \sqrt{3}|\frac{1}{2}, \frac{1}{2}\rangle + |-\frac{1}{2}, \frac{3}{2}\rangle\right) \\
|J = 3, m_J = 0\rangle &= \frac{1}{\sqrt{20}}\left(|\frac{3}{2}, -\frac{3}{2}\rangle + 3|\frac{1}{2}, -\frac{1}{2}\rangle + 3|-\frac{1}{2}, \frac{1}{2}\rangle + |-\frac{3}{2}, \frac{3}{2}\rangle\right) \\
|J = 3, m_J = -1\rangle &= \frac{1}{\sqrt{5}}\left(|\frac{3}{2}, -\frac{1}{2}\rangle + \sqrt{3}|-\frac{1}{2}, -\frac{1}{2}\rangle + |\frac{1}{2}, -\frac{3}{2}\rangle\right) \\
|J = 3, m_J = -2\rangle &= \frac{1}{\sqrt{2}}\left(|-\frac{3}{2}, -\frac{1}{2}\rangle + |-\frac{1}{2}, -\frac{3}{2}\rangle\right) \\
|J = 3, m_J = -3\rangle &= |-\frac{3}{2}, -\frac{3}{2}\rangle
\end{aligned} \tag{S8}$$

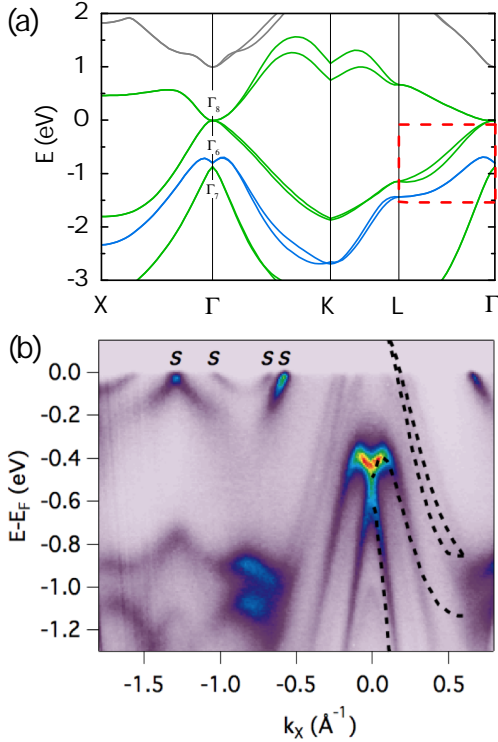


fig. S1. Comparison of YPtBi bulk band structure to ARPES. (a) Calculated band structure of YPtBi obtained using the full potential linearized augmented plane wave method with the Tran-Blaha modified Becke-Johnson exchange-correlation potential (MBJLDA). (b) Results of angle-dependent photoemission spectroscopy (ARPES) measurement done on Bi-terminated (111) surface. The black dashed lines represent the calculated band structure along Γ -L. The chemical potential in ARPES result is about 0.32 eV below that of theoretical result.

ELECTRONIC STRUCTURE

Figure S1 presents the band structure of YPtBi. The calculated band structure of YPtBi shown in panel (a) was obtained using the WIEN2k implementation of the full potential linearized augmented plane wave method

with the Tran-Blaha modified Becke-Johnson exchange-correlation potential (MBJLDA) [40], with spin-orbital coupling included in the calculation. The k -point mesh was taken to be $11 \times 11 \times 11$, and cubic lattice constant $a = 664.0(1)$ pm was obtained from elsewhere [26]. The s -like band Γ_6 lies below the p -like band Γ_8 , reflecting the nontrivial topology, consistent with previous calculations [1-3]. Note the splittings will disappear in a non-relativistic calculation, and also it is common to have these spin splittings vanish at high symmetry points and along high symmetry directions. This is because there are symmetry elements that require band degeneracies, which are removed when we move away from these special points. This splitting evidences a $j=3/2$ analogue of anti-symmetric spin-orbit coupling (ASOC) due to broken inversion symmetry, similar to Rashba spin-orbit coupling in tetragonal systems [25].

Figure S1(b) shows an ARPES high symmetry valence band dispersion image at $h\nu = 86$ eV for the Bi-terminated (111) surfaces of YPtBi, acquired at beamline 4.0.3 of the Advanced Light Source at $T = 30$ K. Numerous bands are observed to cross the Fermi-level (E_F) from the zone boundary to normal emission. Consistent with ARPES measurements of LuPtBi and GdPtBi [23], the photon energy dependence of most of these bands follows strong vertical streaks along k_z indicative of 2D surface states. Theoretical slab calculations [23] have determined that the surface states, labeled s in fig. S1(b), originate from a Bi-terminated (111) cleavage plane, and that they are of non-topological origin owing to an even number of E_F -crossings with the surface Brillouin zone. Aging of the surface in a poorer storage vacuum for a week is observed to suppress all the surface states and leave a single fuzzy broad hole-band feature that reaches to E_F . A similar inner-hole band pocket was also observed as a single-band with weak intensity in LuPtBi and GdPtBi [23] and assumed to be a pair of nearly degenerate bands from comparison to their slab calculations.

A characteristic Rashba-like splitting of two hole bands is shown in fig. S1(b) at ≈ 0.5 eV binding energy which

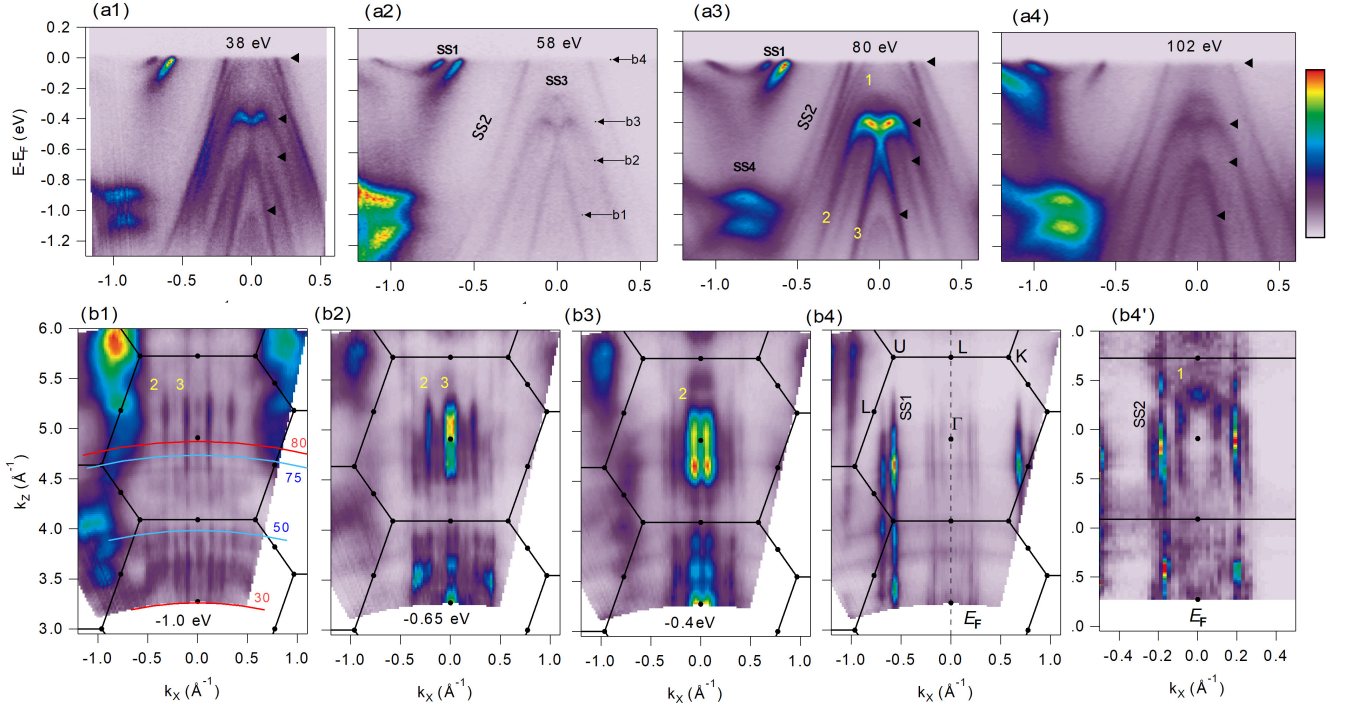


fig. S2. Photon dependence of Bi-terminated YPtBi(111). (a) Normal emission band dispersion images at select photon energies. (b) k_x - k_z intensity maps at select binding energies as marked by arrows in panel (a2) and with overplotted Brillouin zone boundaries with (111) along k_z . The ARPES data are converted to k_z using an inner potential parameter of 15 eV. Red (blue) arcs in panel (b1) indicate the photon energy ranges probed by Ref. [23] (30-80 eV) and by Ref. [24] (50-75 eV). Bi-termination surface states (SS1-SS4) and other bulk-derived states with band-bending-induced 2D character (1-3) are labeled in both (a) and (b).

also appear in bulk band structure calculations, but at an energy of ≈ -0.8 eV below E_F . Shifting the theory Γ -L bands to higher energy by ≈ 0.3 eV to align to the Rashba-like split bulk bands, as shown in overplotted dashed lines, causes two other nearly-degenerate hole-like bulk bands that originally just touch E_F at a semimetal point, to form a hole-pocket. This large 0.3 eV chemical potential shift in the ARPES measurement, relative to the theory calculation, reflects a possible charge imbalance at the cleaved surface and resultant band bending relative to the bulk.

In order to determine the bulk or surface character of the ARPES bands, we have performed photon energy dependence on Bi-terminated (111) surfaces of YPtBi. The photon dependent ARPES map cuts shown in fig. S2 reveal two different kinds of surface states: (i) surface-localized Bi-terminated dangling bond states and (ii) bulk-derived states that acquire 2D character from the p -type surface band bending that results from the Bi-termination charge balance and pinning of the chemical potential at the surface. The Bi surface states, SS1-SS4, exhibit vertical streaks along k_z in the constant binding energy intensity cuts, e.g. SS1 in (b4) and SS2 in (b4'), with a strong presence at all photon energies. This lack of k_z -variation with weak intensity variation uncorrelated

to the bulk Brillouin zone (BZ) reflects a 2D origin from the top few layers of the surface, e.g. narrowly confined Δz causes extended Δk_z . Other states labeled (1-3) in fig. S2 exhibit a distinctly different intensity profile of finite segments of strong intensity along k_z centered on the bulk Γ -point, and with length $< 1/2$ the height of the overplotted (111)-oriented BZ boundaries. This finite k_z length of the strong photoemission intensity reflects a deeper depth origin ($\Delta z \approx 2\pi/\Delta k_z$) of these states. e.g. at least two (111) unit cells in real space.

This distinct intensity behavior as a function of photon energy was not previously revealed in ARPES studies with limited photon energy ranges of 30-80 eV in Ref. [23] and 50-75 eV in Ref. [24] as plotted in fig. S2 (b1). This behavior is consistent with bulk-derived quantum well states with a depth penetration that is determined by the z -profile of the band-bending potential. Furthermore, a finite gap between bands 2 and 3 at $k_x = 0$ is suggested by the dispersion images in panels (a1,a4) at 38 eV and 102 eV, consistent with the bulk theory band structure shown in fig. S1. The filling in of the gap and full Rashba-like appearance is then conjectured to arise from a topological surface state with Dirac crossing that connects between the bulk-like bands 2 and 3. This scenario is consistent with the theoretical calculations Ref. [24].

The experimental quantum oscillation frequency of $F \approx 45$ T [4] corresponds to a cross sectional area of a hypothetical spherical Fermi surface $A_F \approx 0.43$ nm⁻² and a $k_F \approx 0.037$ Å⁻¹, using the Onsager relation $F = \phi_0 A_F / 2\pi^2$ where $A_F = \pi k_F^2$ and $\phi_0 = 2.07 \times 10^{-7}$ G cm⁻², which is much smaller than the ARPES k_F values in fig. S1(b) of ≈ 0.1 Å⁻¹. This supports the scenario of a charge imbalance at the surface and band bending with the bulk chemical potential only ≈ 35 meV below the hole-band maximum. This justifies the vertical energy shift used to match to the calculated DFT band structure and quantum oscillations experiments.

$j = 3/2$ $\mathbf{k} \cdot \mathbf{p}$ MODEL

We treat the ASOC as a perturbation of the Luttinger-Kohn model, which has doubly-degenerate eigenenergies

$$\epsilon_{\mathbf{k},\pm} = \left(\alpha + \frac{5}{4}\beta \right) |\mathbf{k}|^2 \pm \beta \sqrt{\sum_i \left[k_i^4 + \left(\frac{3\gamma^2}{\beta^2} - 1 \right) k_i^2 k_{i+1}^2 \right]} \quad (\text{S9})$$

Due to the presence of time-reversal and inversion symmetry for $\delta = 0$, the eigenstates can be labelled by a pseudospin-1/2 index. Proceeding via degenerate perturbation theory, we now include the ASOC by projecting it into the pseudospin basis for each band, hence obtaining

$$\tilde{\Delta}(\mathbf{k}) = \Delta_s \begin{pmatrix} 0 & 0 & 0 & 1 \\ 0 & 0 & -1 & 0 \\ 0 & 1 & 0 & 0 \\ -1 & 0 & 0 & 0 \end{pmatrix} + \Delta_p \begin{pmatrix} \frac{3}{4}k_- & \frac{\sqrt{3}}{2}k_z & \frac{\sqrt{3}}{4}k_+ & 0 \\ \frac{\sqrt{3}}{2}k_z & \frac{3}{4}k_+ & 0 & -\frac{\sqrt{3}}{4}k_- \\ \frac{\sqrt{3}}{4}k_+ & 0 & -\frac{3}{4}k_- & \frac{\sqrt{3}}{2}k_z \\ 0 & -\frac{\sqrt{3}}{4}k_- & \frac{\sqrt{3}}{2}k_z & -\frac{3}{4}k_+ \end{pmatrix} \quad (\text{S12})$$

where $k_{\pm} = k_x \pm ik_y$. This constitutes a mixed state involving s -wave singlet pairing with strength Δ_s and p -wave *septet* pairing with strength Δ_p . The gap near the Fermi energy can be found by projecting Eq. (S12) into the effective pseudospin-1/2 bands, yielding

$$\Delta_{\text{eff},\pm} = [\Delta_s + (\Delta_p/\delta)(\mathbf{g}_{\mathbf{k},\pm} \cdot \hat{\mathbf{s}})] i\hat{s}_y \quad (\text{S13})$$

This describes a mixture of pseudospin-singlet and pseudospin-triplet pairing. Importantly, the \mathbf{d} -vector of the effective pseudospin-triplet pairing is parallel to the ASOC vector $\mathbf{g}_{\mathbf{k},\pm}$. As pointed out by Frigeri *et al.* [9], this alignment makes the pseudospin-triplet component immune to the pair-breaking effect of the ASOC; for sufficiently large ASOC, it is the only stable odd-parity gap. If the singlet state is subdominant, the resulting gap dis-

two effective pseudospin-1/2 Hamiltonians

$$H_{\text{eff},\pm} = \epsilon_{\mathbf{k},\pm} \hat{s}_0 + \mathbf{g}_{\mathbf{k},\pm} \cdot \hat{\mathbf{s}} \quad (\text{S10})$$

where \hat{s}_μ are the Pauli matrices for the pseudospin, and the vector $\mathbf{g}_{\mathbf{k},\pm} = -\mathbf{g}_{-\mathbf{k},\pm}$ represents the effective ASOC in the pseudospin-1/2 basis of the band $\epsilon_{\mathbf{k},\pm}$. The expression for $\mathbf{g}_{\mathbf{k},\pm}$ is complicated and depends upon the choice of pseudospin basis; an analytic expression for $|\mathbf{g}_{\mathbf{k},\pm}|$ is given elsewhere [13]. The effective pseudospin-1/2 Hamiltonians can be diagonalized by going over to the helicity basis, yielding dispersions $E_{\mathbf{k},\eta=\pm,\nu=\pm} = \epsilon_{\mathbf{k},\eta} + \nu|\mathbf{g}_{\mathbf{k},\eta}|$, where the values of η and ν are independent of one another. In particular, the two spin-split Fermi surfaces are labelled by opposite values of ν . This approximation is in excellent agreement with the exact solutions of the $\mathbf{k} \cdot \mathbf{p}$ for small antisymmetric SOC.

In weak-coupling Bogoliubov-de Gennes theory the pairing is modelled by a term in the Hamiltonian of the form

$$H_{\text{pair}} = \sum_{\mathbf{k}} \sum_{j,j'=-3/2}^{3/2} \left\{ \Delta_{j,j'}(\mathbf{k}) c_{\mathbf{k},j}^\dagger c_{-\mathbf{k},j'}^\dagger + \text{H.c.} \right\} \quad (\text{S11})$$

We restrict our attention to gaps in the A_1 irreducible representation of the T_d point group (i.e. with the full symmetry of the lattice). Allowing pairing in at most a relative p -wave (assuming quasi-local interactions are responsible for the superconductivity, higher-order momentum-dependence is unlikely [36]), we have the general gap

plays line nodes on one of the spin-split Fermi surfaces.

Although the nodal gap prevents us from defining a global topological invariant, the nodal lines themselves represent a nontrivial topological defect in the Brillouin zone. Specifically, the Bogoliubov-de Gennes Hamiltonian $H_{BdG}(\mathbf{k})$ belongs to Altland-Zirnbauer class DIII, which implies that it can be brought into off-diagonal form. This allows us to define the winding number

$$W_{\mathcal{L}} = \frac{1}{2\pi} \text{Im} \oint_{\mathcal{L}} d\ell \text{Tr} \{ \nabla_\ell \ln(D_{\mathbf{k}}) \} \quad (\text{S14})$$

where $D_{\mathbf{k}}$ is the upper off-diagonal block of the Hamiltonian [8]. The winding number $W_{\mathcal{L}}$ takes an integer value along any closed path \mathcal{L} in the Brillouin zone that does not intersect a gap node. Moreover, it is only nonzero if

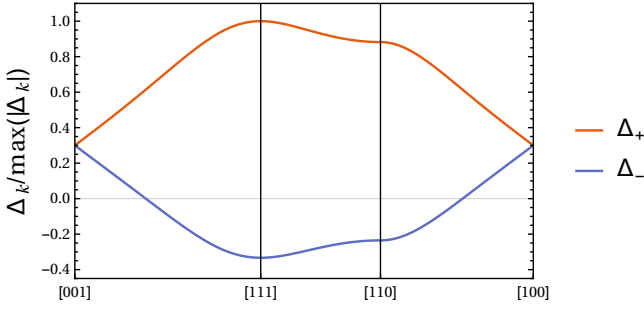


fig. S3. Normalized magnitude of each gap $\Delta_k/\max(|\Delta_k|)$ along high symmetry points is presented for full gap and nodal gap in red and blue, respectively. Whereas the fully gapped branch (red) contributes only thermally activated quasiparticles at low temperatures, the line-node branch (blue) manifests a linear temperature variation of the London penetration depth $\Delta\lambda \propto T$, consistent with experimental observations in YPtBi.

the path \mathcal{L} encircles a line node, defining the topological charge of the node which in our case evaluates to ± 1 . This topological charge ensures the existence of a nondegenerate zero-energy surface flat band within the projection of the line node in the surface Brillouin zone [8].

Some alternatives to the mixed singlet-septet state proposed here should be noted. In particular, for purely local pairing interactions, there are five additional s -wave states with quintet total angular momentum [13]. Within a weak-coupling theory, these combine to give time-reversal symmetry-breaking states gaps with Weyl point nodes, and in some cases also line nodes. While such pairing states also topological, they do not yield robust zero-energy surface flat bands [37].

Figure S3 shows distribution of gap amplitudes $\Delta_k/\max(|\Delta_k|)$ along high symmetry points on the spin-split Fermi surfaces of YPtBi, with a full gap on the outer Fermi surface and gap with line nodes on the inner Fermi surface (see Fig. 4 in the main text for the gap structure on the entire Fermi surface). Whereas the fully gapped branch (Δ_+) contributes only thermally activated quasiparticles at low temperatures, the line-node branch (Δ_-) manifests a linear temperature variation of the London penetration depth $\Delta\lambda \propto T$, consistent with experimental observations in YPtBi.

LONDON PENETRATION DEPTH AND SUPERFLUID DENSITY

The temperature variation of London penetration depth is intimately related to the superconducting order parameter Δ . Within a weak coupling Eilenberger quasiclassical formulation with the perturbation theory

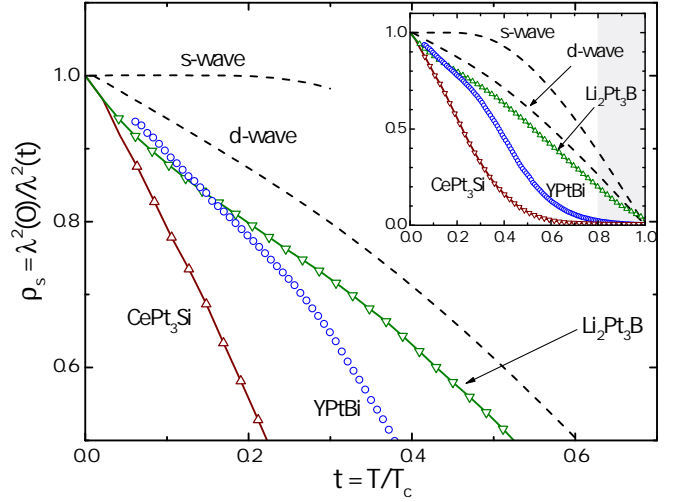


fig. S4. Superfluid density in YPtBi and other well-known superconductors. The normalized superfluid density was calculated by using a relation, $\rho_s = \lambda^2(0)/\lambda^2(T)$ where $\lambda(0) = 1.6\mu\text{m}$ [30]. Theoretical singlet s -wave and d -wave are shown in dashed lines, and experimental data from noncentrosymmetric superconductors are shown in triangle symbols for CePt₃Si (Ref. [33]) and Li₂Pt₃B (Ref. [34]).

of a weak magnetic field [27]

$$(\lambda^2)_{ik}^{-1} = \frac{16\pi^2 e^2 T}{c^2} N(0) \sum_{\omega} \left\langle \frac{\Delta^2 v_i v_k}{(\Delta^2 + \hbar^2 \omega^2)^{3/2}} \right\rangle \quad (\text{S15})$$

where $N(0)$ is the total density of states at Fermi level per spin, v is the Fermi velocity, and ω is the Matsubara frequency. Measurement of the London penetration depth utilizes a small excitation field $H_{ac} < 20$ mOe, so the Eq. (S15) is valid in absence of H_{dc} .

In an s -wave superconductor, an exponential behavior of $\Delta\lambda(T)/\lambda(0) = \sqrt{\pi\Delta_0/2k_B T} \exp(-\Delta_0/k_B T)$ can be deduced from Eq. (S15) for a constant gap $\Delta = \Delta_0$, i.e., at low temperatures $T < T_c/3$, while in a d -wave superconductor $\Delta\lambda(T)$ varies linearly with temperature as $\Delta\lambda(T) = \frac{2\lambda(0)\ln 2}{\eta\Delta_0} T$, at sufficiently low temperatures in a clean sample [31]. Here, η is the angular slope parameter near the node, e.g., $\eta = 2$ for a d -wave gap $\Delta = \Delta_0(k_x^2 - k_y^2)$. To compare the experimental result for YPtBi to the d -wave gap expectation, one can fix the temperature power of $\Delta\lambda(T)$ to $n = 1$ and obtain a slope prefactor $A = 1.5 \mu\text{m}/\text{K}$ from fitting, yielding $2\Delta_0/k_B T_c \approx 4/\eta$. Fixing $\eta = 2$ for the d -wave case gives $2\Delta_0 \approx 2k_B T_c$, which is slightly smaller than the weak-coupling BCS value of $2\Delta_0 = 3.52k_B T_c$.

The normalized superfluid density in YPtBi is calculated by using a relation, $\rho_s = \lambda^2(0)/\lambda^2(T)$. Here we used $\lambda(0) = 1.6 \mu\text{m}$ determined by μSR experiments [28]. The calculated ρ_s is compared to that of well-known superconductors in fig. S4. Theoretical ρ_s of singlet s -wave and d -wave superconductors are shown in dashed

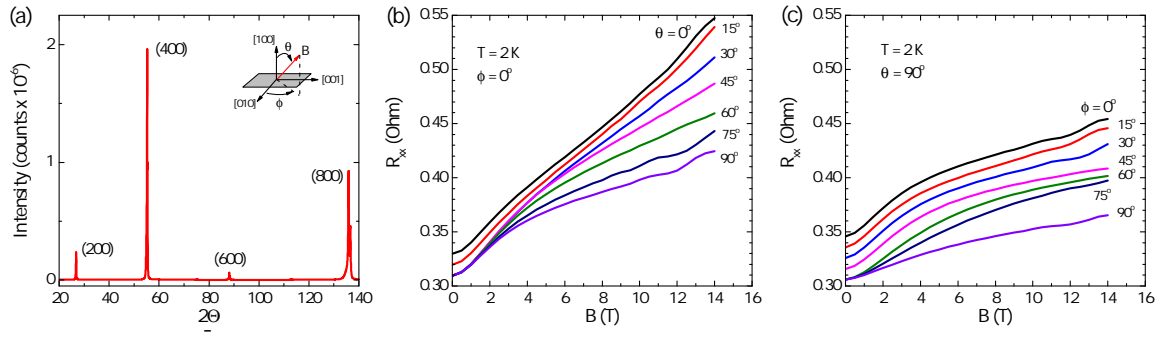


fig. S5. Angle-dependent magnetoresistance in YPtBi. (a) Single crystal x ray diffraction pattern of (100) surface of YPtBi used for angle-dependent quantum oscillation experiments. A schematic defines two controlled angles θ and ϕ . Angle-dependent magnetoresistance (b) with varying θ at fixed $\phi = 0^\circ$ and (c) with varying ϕ at fixed $\theta = 90^\circ$. Shubnikov-de Haas quantum oscillations are evident in most of the orientations.

lines, and the experimental ρ_s from two other noncentrosymmetric superconductors, CePt₃Si [33] and Li₂Pt₃B [34], are shown in triangle symbols. Whereas the singlet *s*-wave does not exhibit noticeable temperature-variation up to $0.2T_c$, the other nodal superconductors show nearly linear temperature-dependence. The superfluid density in CePt₃Si is most compatible with an order parameter with two vector components [33] and that in Li₂Pt₃B is consistent with a spin singlet-triplet mixed pairing with the triplet component being dominant [34]. Interestingly, the superfluid density in YPtBi has similar behavior to that of the other noncentrosymmetric superconductors, and is consistent with multigap, line-nodal superconducting order parameter.

We note that the value of penetration depth rapidly approaches the characteristic size of the sample R (see Methods for detail) near T_c because of large $\lambda(0)$ in YPtBi ($\Delta\lambda(T) \propto \lambda(0)$). In this temperature range, the measurement is in an extreme sample size-limiting effect, and the temperature-variation of both $\Delta\lambda$ and ρ_s in YPtBi are severely affected by this effect. Therefore, the superfluid density near T_c should not be taken seriously, and we highlighted the problematic region in the inset of fig. S4.

ANGLE-DEPENDENT MAGNETORESISTANCE

Angle-dependent magnetoresistance was measured to study the spin-split Fermi surface of YPtBi. A sample was cut out of (100) plane confirmed by a single-crystal diffraction pattern as shown in fig. S5(a). The angle-dependence of the longitudinal magnetoresistance R_{xx} was measured by using a single-axis rotator at various orientations with two controlled angles θ and ϕ defined in fig. S5(a). Panel (b) shows angle-dependent magnetoresistance data with varying θ from 0° to 90° at $\phi = 0^\circ$. At most of the angles, Shubnikov-de Haas (SdH) quantum oscillations are visible on smoothly increasing

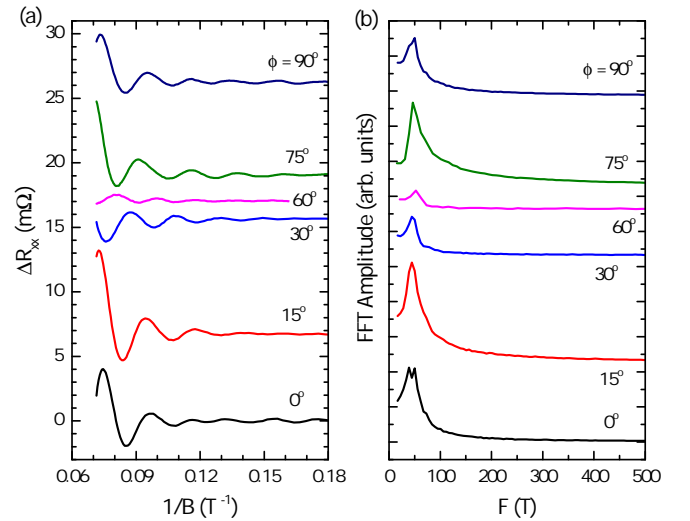


fig. S6. Angle-dependent frequency of Shubnikov-de Haas quantum oscillation in YPtBi. (a) SdH quantum oscillations extracted from the magnetoresistance at selected ϕ angles with fixed $\theta = 90^\circ$. (b) Fast Fourier transform spectra obtained from the quantum oscillations shown in (a). The angles are defined in fig. S5.

magnetoresistance. Similar experiments with varying ϕ from 0° to 90° at $\theta = 90^\circ$ were done and presented in fig. S5(c). In both configurations, SdH oscillations show angle-dependence where the amplitude and phase changes at different orientations of the applied magnetic field implying the SdH consists of multiple frequencies with varying frequencies and relative phases. The oscillations at 0° and 90° in both configurations appear the same, confirming the assignment of crystallographic orientation in the schematic.

Figure S6(a) shows the SdH quantum oscillations obtained from the magnetoresistance data in fig. S5(c). The angle-dependence of SdH oscillation is clear while the oscillations at $\phi = 0^\circ$ and 90° oscillations are nearly identical in both of which display a beating node around $B^{-1} = 0.12 \text{ T}^{-1}$. We employ the fast Fourier transform

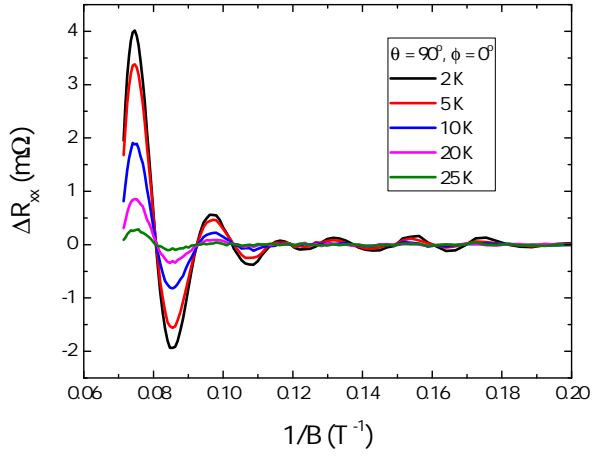


fig. S7. Temperature-dependent quantum oscillations with $\theta = 90^\circ$ and $\phi = 0^\circ$. The angles are defined in fig. S5.

(FFT) to determine the frequency for several selected angles. The FFT-spectra are shown in fig. S6(b). At first glance, the spectrum shows a broad peak around $F = 46$

T at all selected angles. The angular variation of the determined frequencies is presented in Fig. 3(b) in the main text. In some orientations, it shows a broad feature with double peaks, and the two peaks are clearly resolved in the data for $\phi = 0^\circ$ with two frequencies of 39 ± 3 T and 50 ± 3 T where the error bar is the frequency resolution of FFT. We attributed the observation of two frequencies to the existence of spin-split Fermi surfaces. Using a theory by Mineev and Samokhin [22], the estimated energy of spin-orbit coupling is about 1 meV when Zeeman interaction is much smaller than spin-orbit interaction.

To learn the nature of the Fermi surfaces associated with two resolved frequencies, we measured temperature-dependent SdH quantum oscillations with field along [010], i.e., $\theta = 90^\circ$ and $\phi = 0^\circ$. Temperature-dependent SdH oscillations are displayed in fig. S7, FFT-spectra of which are presented in Fig. 3(c) in the main text. We determined effective mass from temperature dependence of the amplitude by using the Lifshitz-Kosevich theory as shown in Fig. 3(d) in the main text. They have nearly identical effective mass as expected for spin-split Fermi surfaces.